Data-driven closures for the dynamic mode decomposition using quadratic manifolds

Aniketh Kalur [*], Patrick Mortimer[†], Jayant Sirohi[‡], Rudy Geelen[§], and Karen Willcox[¶]
University of Texas at Austin, Austin, TX, 78712

This paper presents a nonlinear dimensionality reduction technique for obtaining nonlinear reduced-order models. The approach is data-driven and flexible in the types of data that may be used. Specifically, the reduced-order model is identified using training data that may be generated via simulation, experimental observations, or a combination of both. The first step in the approach is to collect a training dataset that comprises state solutions and/or observations that are representative of the dynamics to be approximated. The second step is to derive an intermediate linear model using the dynamic mode decomposition (DMD). This linear model is chosen to have a dimension that retains all available information from the dataset. The third step is to perform nonlinear dimension reduction, by retaining a limited number of modes in the DMD model and adding a quadratic closure term to represent the effects of the truncated modes. This quadratic closure term is inferred from the original dataset by solving a linear least-squares regression problem. Reduced-order modeling using the proposed approach is demonstrated in both the low-data regime and sufficient-data regime. In a low-data regime, the proposed approach yields improvement in predicting dynamics beyond the training dataset, when compared to other linear dimensionality reduction techniques. We demonstrate this using an illustrative Burgers' equation numerical example. An application example considers an experimental dataset of time-resolved particle image velocimetry of rotorcraft blades in hover mode. Applying the proposed approach to this experimental dataset leads to effective nonlinear reduced models of the rotor blade interaction with the surrounding air.

Nomenclature

$\mathbf{F}$ nonlinear map of state transition

$\mathbf{x}$ N-dimensional full-order state vector

---

*Postdoctoral Fellow, Oden Institute for Computational Engineering and Sciences, AIAA Member.
†Graduate student, Aerospace Engineering and Engineering Mechanics
‡Professor, Aerospace Engineering and Engineering Mechanics
§Postdoctoral Fellow, Oden Institute for Computational Engineering and Sciences
¶Director, Oden Institute for Computational Engineering and Sciences, Professor, Aerospace Engineering and Engineering Mechanics, AIAA Fellow

$\widetilde{\mathbf{x}}$	ℓ-dimensional intermediate state vector
$\widehat{\mathbf{x}}$	r-dimensional reduced-order state vector
$\mathbf{X}, \mathbf{X}'$	snapshot matrices
N	full-order model state dimension
ℓ, r	reduced-order model state dimensions
$\mathbf{A}$	linear system matrix
$\widetilde{\mathbf{A}}$	rank ℓ approximation of $\mathbf{A}$
$\widehat{\mathbf{A}}, \widehat{\mathbf{H}}$	reduced-order system operators
$\mathbf{U}, \mathbf{\Phi}$	left singular vectors
$\mathbf{V}, \mathbf{\Psi}$	right singular vectors
$\mathbf{\Sigma}, \mathbf{\Theta}$	singular value matrix
$\mathcal{E}$	linear projection error
$\overline{\mathbf{\Phi}}$	shape factor for closure term
γ	regularization factor

I. Introduction

Partial differential equations (PDEs) model the governing dynamics of many physical sciences (fluid flows, solid mechanics, etc.) and engineered systems (airplanes, combustion engines, rotorcraft, etc.). Numerical models of these PDEs typically result in high-dimensional nonlinear systems that are computationally expensive to solve. Reduced-order models (ROMs) are often used as approximations, such that the physical system's dynamics are approximated at reduced computational costs. Deriving these ROMs requires training data; in most applications, these data are generated by solving the original expensive PDE model for representative conditions. The generation of sufficient training data can become computationally prohibitive at the scale needed for many practical applications. This paper considers the derivation of ROMs in settings where only a small amount of data is available to train the ROM. These data may be generated numerically and/or experimentally.

ROMs developed using projection-based methods have been used extensively in various applications, especially in fluid flows [1]. An essential aspect of projection-based ROMs is finding an appropriate basis that defines a low-dimensional subspace onto which the high-dimensional system is projected [2]. The widely used proper orthogonal decomposition (POD) [3] provides a basis for modal decomposition via an optimal representation of the kinetic energy included in a training dataset [4]. Another approach to data-driven model reduction is the dynamic mode decomposition (DMD) [5]; here, nonlinear system observables are used to obtain an approximation of the Koopman operator, an infinite dimensional linear operator. DMD-based methods have shown great success in developing

ROMs and uncovering underlying physics [5–10]. Other successful recent methods for data-driven reduced-order modeling include the sparse identification of nonlinear dynamics (SINDy) for ordinary and partial differential equations [11, 12] and operator inference for non-intrusive projection-based model reduction [13–16]. Despite the success of these techniques for challenging problems, their dependence on linear dimensionality reduction compromises their effectiveness in problems characterized by strong nonlinearity, especially when training data are sparse.

Recent years have seen growth in nonlinear dimensionality reduction techniques for physics-based ROMs. For instance, convolutional autoencoders have provided an approach for identifying a nonlinear manifold on which the system's dynamics can be represented more accurately than for the linear subspace defined by a similar POD compression [17]. However, as the number of trainable parameters scales with the dimensionality of input data and the complexity of the neural network architecture, these autoencoder models quickly become computationally intractable even for two-dimensional PDE settings [18]. Recent approaches, see [19], exploit the benefits of both POD and autoencoder approaches while mitigating potential limitations, including the computational cost associated with training and testing. In parallel to these developments, quadratic solution manifolds have emerged as a promising tool for nonlinear dimensionality reduction in projection-based model reduction [16, 20–22]. The construction of a quadratic manifold scales to large-scale problems and remains interpretable when combined with a projection-based reduced-order model.

In [16], it was noted that projection onto a quadratic manifold could be interpreted as a form of closure modeling that accounts for the effects of truncated modes. It is well documented in the literature that errors due to truncation compromise the robustness and effectiveness of the resulting ROMs, especially for applications that involve future-state prediction and rely on the long-term stability of ROMs [23, 24]. In [25], the authors propose a data-driven closure modeling approach using sparse regression and neural networks. Further, closure models have also been introduced to correct for specific errors that may arise due to truncation, for example, to account for truncation of low-energy modes (especially in POD-based ROMs) [26], to account for multi-scale features [27], and to account for parameter variations using learning-based closure models [28]. A detailed list of closure models for ROMs can also be found in [26].

In this work, we draw on three concepts in data-driven modeling: (1) a best-fit linear evolution operator that advances the states of nonlinear dynamical systems forward in time, (2) a dimensionality reduction step to exploit low-dimensional structure in data, and (3) a nonlinear dimensionality reduction via a quadratic manifold that introduces a closure term to account for the effects of truncated modes. The resulting algorithm is scalable to large-scale systems and produces a low-dimensional ROM with a linear-quadratic structure.

This paper is organized as follows. Section II provides a mathematical overview of linear dimensionality reduction, motivates the need for closure models, and introduces the data-driven approach to identify the closure term. We demonstrate how a nonlinear reduction with quadratic manifolds produces a linear-quadratic model and how adding the quadratic closure term helps minimize projection error encountered in linear dimensionality reduction. We illustrate this using a low-dimensional example of cylinder vortex shedding. Section III demonstrates the proposed method's

improved future state prediction capabilities on the low-viscosity Burgers equation, and an experimental dataset obtained for modeling the flow field of a hovering helicopter rotor. Finally, we provide concluding remarks in section IV.

II. Approach
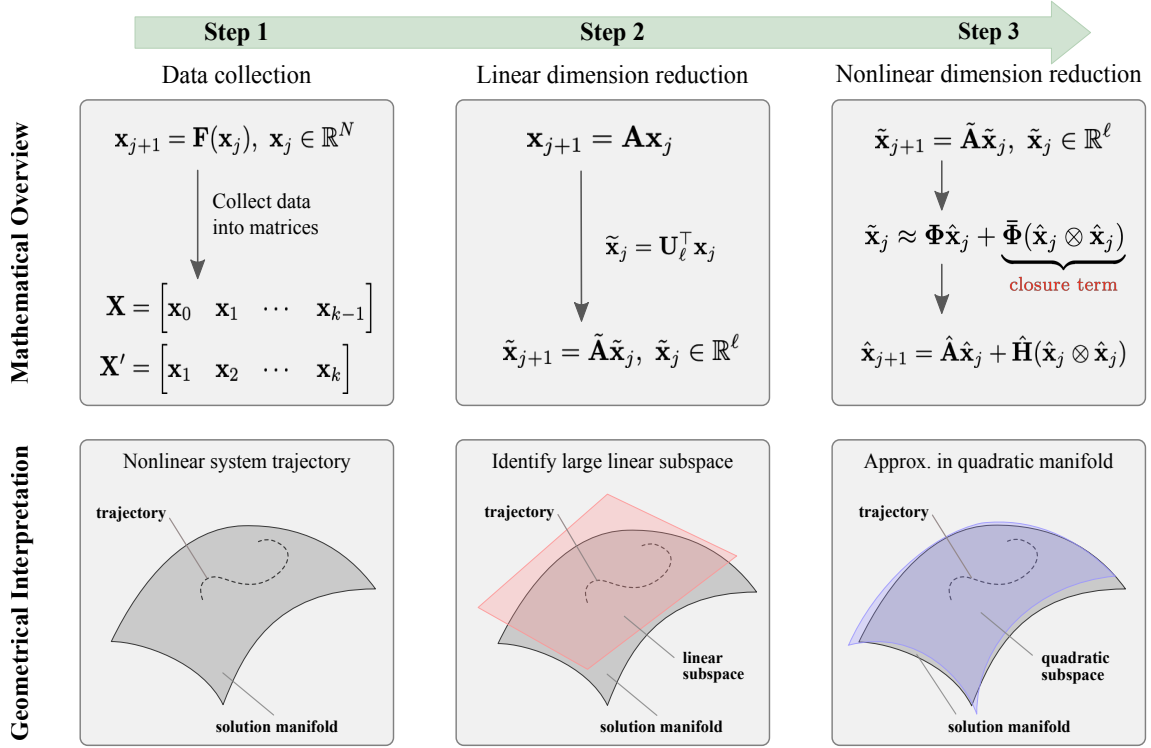
Fig. 1 The figure highlights the three-step process to obtain a DMD model with quadratic closure. The upper gray blocks shows the overview of the mathematical process involved, while the lower gray blocks provides a geometrical interpretation of each step's results.

Fig. 1 provides an overview of the approach that is presented in this section. Consider a discrete-time nonlinear system of the form

$$\mathbf{x}_{j+1} = \mathbf{F}(\mathbf{x}_j), \tag{1}$$

where $\mathbf{x}_j \in \mathbb{R}^N$ is the state of the system at time t_j and $\mathbf{F} : \mathbb{R}^N \mapsto \mathbb{R}^N$ is the nonlinear map that propagates the system from time t_j to t_{j+1}. We target problems for which the system in Eq. (1) is high-dimensional; that is, the number of degrees of freedom $N \gg 1$. Given the initial condition $\mathbf{x}_0$, we collect the system's trajectory data for the duration of the time period of interest, such that time index $j = 0, 1, \cdots, k$.

A. Linear dimensionality reduction using dynamic mode decomposition

The system in Eq. (1) is nonlinear; we will first obtain an intermediate linear approximation of the system using DMD. To obtain this linear map from data, we collect the system trajectories into two time-shifted snapshot matrices

$\mathbf{X} \in \mathbb{R}^{N \times k}$ and $\mathbf{X}' \in \mathbb{R}^{N \times k}$ given as

$$\mathbf{X} = \begin{pmatrix} | & | & & | \\ \mathbf{x}_0 & \mathbf{x}_1 & \cdots & \mathbf{x}_{k-1} \\ | & | & & | \end{pmatrix}; \qquad \mathbf{X}' = \begin{pmatrix} | & | & & | \\ \mathbf{x}_1 & \mathbf{x}_2 & \cdots & \mathbf{x}_k \\ | & | & & | \end{pmatrix}, \tag{2}$$

where typically $N > k$ for high-dimensional problems. In Eq. (2), each column in the matrices is a sampled state vector $\mathbf{x}_j$ at time index j. One approach to obtaining a best-fit linear operator for this dataset is to solve for a reduced-rank approximation $\widetilde{\mathbf{A}} \in \mathbb{R}^{\ell \times \ell}$ using the DMD algorithm [5, 29, 30].

The POD modes are obtained by decomposing the snapshot matrix using the singular value decomposition (SVD) such that $\mathbf{X} = \mathbf{U}\boldsymbol{\Sigma}\mathbf{V}^{\top}$. The singular value matrix $\boldsymbol{\Sigma}$ is a diagonal matrix containing the singular values $\sigma_1, \sigma_2, \cdots$. There are at most $\ell \leq \min(N, k)$ non-zero singular values, ordered as $\sigma_1 \geq \sigma_2 \cdots \geq \sigma_\ell > 0$. We note that in the low-data regime, that is when the number of snapshots k is small and $k \ll N$, we expect $\ell = k$. In this first linear dimensionality reduction step, we retain ℓ left singular vectors to form the POD basis. This retains the maximum information available in the data by discarding only the modes associated with zero singular values. The DMD best-fit rank-ℓ linear operator is then given by

$$\widetilde{\mathbf{A}} = \mathbf{U}_\ell^{\top} \mathbf{X}' \mathbf{V}_\ell^{\top} \boldsymbol{\Sigma}_\ell^{-1}, \tag{3}$$

where $\mathbf{U}_\ell$ are the dominant ℓ POD modes of the snapshot matrix $\mathbf{X}$.

Obtaining a reduced-rank approximation $\widetilde{\mathbf{A}}$ defines an intermediate linear system,

$$\widetilde{\mathbf{x}}_{j+1} = \widetilde{\mathbf{A}}\widetilde{\mathbf{x}}_j, \quad \widetilde{\mathbf{x}}_j \in \mathbb{R}^{\ell}. \tag{4}$$

The goal now is to reduce this system to a compact representation of dimension $r \leq \ell$. In many cases, an rth-order linear DMD representation will be adequate; however, in some cases, even choosing $r = \ell$ leads to a linear ROM with limited predictive capability. One is faced with a key tension: choosing r to be small (i.e., retaining only the dominant modes) leads to a ROM that is robust and stable, but that is inaccurate due to the effect of truncated modes. Increasing r (i.e., $r \rightarrow \ell$) reduces the projection error of representation in the linear subspace, but as higher order modes are included, one often obtains a ROM that in unstable and/or lacks robustness.

This motivates our approach: we approximate the ℓth-order system (4) in a quadratic manifold, following the approach of [16]. In doing so, our reduced-order state is represented in an rth-order space comprised of the dominant modes, while the truncated modes are accounted for through the quadratic closure term. The closure term allows for the

5

ROM's dynamics to include components in all ℓ modes present in the snapshot data, but in contrast to a direct ℓth-order DMD approximation, the modal coefficients for the higher-order modes are constrained (as quadratic functions of the modal coefficients of the first r modes). In our numerical results we observe that this approach permits us to achieve accurate, stable ROMs in cases where DMD fails to provide accurate predictions outside of the training regime.

B. Data-driven closure modeling to minimize projection error

An rth-order linear DMD ROM would take the form

$$\widehat{\mathbf{x}}_{j+1} = \widehat{\mathbf{A}}\widehat{\mathbf{x}}_j, \quad \widehat{\mathbf{x}}_j \in \mathbb{R}^r, \tag{5}$$

where $\widehat{\mathbf{A}} \in \mathbb{R}^{r \times r}$ is the $r \times r$ upper block of $\widetilde{\mathbf{A}}$. Following the ideas in [16], we employ a quadratic closure term that accounts for the remaining $\ell - r$ modes that have been truncated compared with the DMD system (4). Notionally, one can consider the closure term to provide a mapping between the truncated state $\widehat{\mathbf{x}}_j \in \mathbb{R}^r$ and the DMD state $\widetilde{\mathbf{x}}_j \in \mathbb{R}^\ell$, where the mapping takes the form

$$\widetilde{\mathbf{x}}_j \approx \boldsymbol{\Phi}\widehat{\mathbf{x}}_j + \overline{\boldsymbol{\Phi}}(\widehat{\mathbf{x}}_j \otimes \widehat{\mathbf{x}}_j), \quad j = 0, \cdots, k-1. \tag{6}$$

Here, $\boldsymbol{\Phi} = \left[\mathbf{I}_{r \times r} \; \mathbf{0}_{(\ell-r) \times r}^\top\right]^\top \in \mathbb{R}^{\ell \times r}$, so that the term $\boldsymbol{\Phi}\widehat{\mathbf{x}}_j$ yields the ℓth-order vector $[\widehat{\mathbf{x}}_j^\top \; \mathbf{0}_{\ell-r}^\top]^\top$. The term $\overline{\boldsymbol{\Phi}}(\widehat{\mathbf{x}}_j \otimes \widehat{\mathbf{x}}_j)$, with $\overline{\boldsymbol{\Phi}} \in \mathbb{R}^{\ell \times r^2}$, introduces components of the solution in the directions of the neglected $\ell - r$ modes. Important to note is that these $\ell - r$ higher-order modes do not have their own free modal coordinates; rather, they are constrained through the term $(\widehat{\mathbf{x}}_j \otimes \widehat{\mathbf{x}}_j)$ to be quadratic products of the first r modal coordinates. The matrix $\overline{\boldsymbol{\Phi}}$ is determined by solving a linear least-squares problem that minimizes the projection error due to the truncation from ℓ to r modes:

$$\overline{\boldsymbol{\Phi}} = \underset{\overline{\boldsymbol{\Phi}} \in \mathbb{R}^{\ell \times r^2}}{\arg\min} \frac{1}{2} \sum_{j=0}^{k-1} \|\widetilde{\mathbf{x}}_j - \boldsymbol{\Phi}\widehat{\mathbf{x}}_j - \overline{\boldsymbol{\Phi}}(\widehat{\mathbf{x}}_j \otimes \widehat{\mathbf{x}}_j)\|_2^2. \tag{7}$$

To simplify the notation, we define matrices $\mathbf{P} = \widetilde{\mathbf{X}} - \boldsymbol{\Phi}\widehat{\mathbf{X}}$ and $\widehat{\mathbf{W}} := \widehat{\mathbf{X}} \odot \widehat{\mathbf{X}}$, where $\odot$ is the column-wise Kronecker product*. While Eq. (7) can be solved, in practical applications the reduced-order snapshot matrices can be ill-conditioned. Hence, we solve a regularized least-squares problem using Tikhonov regularization. The regularized least-squares problem to be solved is

$$\overline{\boldsymbol{\Phi}} = \underset{\overline{\boldsymbol{\Phi}} \in \mathbb{R}^{\ell \times r^2}}{\arg\min} \frac{1}{2}\|\widetilde{\mathbf{X}} - \boldsymbol{\Phi}\widehat{\mathbf{X}} - \overline{\boldsymbol{\Phi}}\widehat{\mathbf{W}}\|_F^2 + \frac{\gamma}{2}\|\overline{\boldsymbol{\Phi}}\|_F, \tag{8}$$

with $\gamma > 0$ is a scalar regularization parameter. Note that by construction, we have $\overline{\boldsymbol{\Phi}}^\top \boldsymbol{\Phi} = \mathbf{0}$ (see [16]).

---

*During implementation, the Kronecker product of a vector can be reduced in size by accounting for repeated entries only once. This reduces the size of the product to $r(r+1)/2$ terms, instead of r^2 terms.

C. Reduced-order models using quadratic closure

Substituting the approximation Eq. (6) into the linear system Eq. (4), employing a Galerkin projection, and using the orthogonality property $\overline{\boldsymbol{\Phi}}^{\top}\boldsymbol{\Phi} = \mathbf{0}$, results in the ROM

$$\widehat{\mathbf{x}}_{j+1} = \widehat{\mathbf{A}}\widehat{\mathbf{x}}_j + \widehat{\mathbf{H}}(\widehat{\mathbf{x}}_j \otimes \widehat{\mathbf{x}}_j), \quad \widehat{\mathbf{x}}_j \in \mathbb{R}^r, \tag{9}$$

where $\widehat{\mathbf{A}} = \boldsymbol{\Phi}^{\top}\widetilde{\mathbf{A}}\boldsymbol{\Phi}$ and $\widehat{\mathbf{H}} = \boldsymbol{\Phi}^{\top}\widetilde{\mathbf{A}}\overline{\boldsymbol{\Phi}}$. It can been seen that the quadratic closure term leads to a ROM that has linear-quadratic form.

The solution for the reduced-order states is obtained in the low-dimensional coordinates by solving Eq. (9) in time. The full-order state approximations of the system can be then computed as

$$\mathbf{x}_j \approx \mathbf{U}_{\ell}\boldsymbol{\Phi}\widehat{\mathbf{x}}_j + \mathbf{U}_{\ell}\overline{\boldsymbol{\Phi}}(\widehat{\mathbf{x}}_j \otimes \widehat{\mathbf{x}}_j) = \mathbf{U}_r\widehat{\mathbf{x}}_j + \mathbf{U}_{\ell}\overline{\boldsymbol{\Phi}}(\widehat{\mathbf{x}}_j \otimes \widehat{\mathbf{x}}_j). \tag{10}$$

The relation in Eq. (10) emphasizes the point that the nonlinear manifold approximation of the solution comprises two parts: the term $\mathbf{U}_r\widehat{\mathbf{x}}_j$ yields an approximation that lies in the subspace spanned by the first r POD modes, while the term $\mathbf{U}_{\ell}\overline{\boldsymbol{\Phi}}(\widehat{\mathbf{x}}_j \otimes \widehat{\mathbf{x}}_j)$ introduces components in the subspace spanned by POD modes $\mathbf{U}_{r+1}\ldots\mathbf{U}_{\ell}$. As noted in Sec. II, this approach may be attractive for problems where directly including the higher order POD modes (i.e., choosing $\mathbf{x}_j \approx \mathbf{U}_{\ell}\widehat{\mathbf{x}}_j$) leads to a ROM that is unstable and/or lacks robustness. The process of obtaining ROMs using DMD combined with a quadratic closure is summarized in Algorithm 1.

Algorithm 1 DMD model reduction with quadratic closures.

Input: Snapshot data $\{\mathbf{x}_1, \mathbf{x}_2, \ldots, \mathbf{x}_k\}$
Output: Reduced model operators $\widehat{\mathbf{A}}, \widehat{\mathbf{H}}$, basis matrices $\mathbf{U}_{\ell}, \overline{\boldsymbol{\Phi}}$

{*Best-fit linear representation of nonlinear dynamics*}
1: Arrange the snapshot data into matrices as per Eq. (2)
2: Compute the singular value decomposition $\mathbf{X} = \mathbf{U}\boldsymbol{\Sigma}\mathbf{V}^{\top}$
3: Set ℓ equal to the number of nonzero singular values of $\mathbf{X}$ (note $\ell \leq \min(N, k)$); define $\mathbf{U}_{\ell}$ as the leading ℓ columns of $\mathbf{U}$
4: Compute the rank-ℓ linear matrix $\widetilde{\mathbf{A}} = \mathbf{U}_{\ell}^{\top}\mathbf{X}'\mathbf{V}_{\ell}\boldsymbol{\Sigma}_{\ell}^{-1}$

{*Learning the quadratic manifold*}
5: Compute reduced snapshots $\widetilde{\mathbf{X}} = \mathbf{U}_{\ell}^{\top}\mathbf{X}$ and $\widehat{\mathbf{X}} = \mathbf{U}_r^{\top}\mathbf{X}$
6: Compute the nonlinear basis matrix $\overline{\boldsymbol{\Phi}}$ by solving Eq. (8) for a given value of γ

{*Define the low-dimensional dynamical system*}
7: Compute the ROM operators $\widehat{\mathbf{A}} = \boldsymbol{\Phi}^{\top}\widetilde{\mathbf{A}}\boldsymbol{\Phi}$ and $\widehat{\mathbf{H}} = \boldsymbol{\Phi}^{\top}\widetilde{\mathbf{A}}\overline{\boldsymbol{\Phi}}$

D. Geometric depiction: A mechanistic low-dimensional model for cylinder flow

In this section, we depict the ideas geometrically using a low-dimensional mechanistic model of a cylinder wake. The model is obtained from [31], where the authors propose a model to highlight the key physical process in the dynamics of cylinder wakes. The three-dimensional model captures empirical behavior from Galerkin-based approaches while providing physical insights into the amplitude selection mechanisms. The model described by ordinary differential equations is

$$\dot{u} = \mu u - v - uw \tag{11}$$

$$\dot{v} = \mu v + u - vw \tag{12}$$

$$\dot{w} = -w + u^2 + v^2. \tag{13}$$

Here, the states of the system $\mathbf{x} = (u, v, w)$ are components of the velocity in x, y, z directions and the constant $\mu = 1/10$. Eq. (13) has an unstable equilibrium point at the origin $\mathbf{x}_e = (u_e, v_e, w_e) = \mathbf{0}$. The system also has a periodic stable solution, which defines a limit cycle of radius $\sqrt{\mu}$ in the $w = \mu$ plane. Therefore, as described in [31], the model mimics the flow around a cylinder with an unstable steady solution and a periodic vortex shedding that is stable. Throughout this section, the numerical simulation is initialized with an initial condition $\mathbf{x}_0 = (0.001, 0, 0.0001)$, and the simulation time is $t = [0, 30]$ with a step size $\Delta t = 0.01$.

Once the system trajectories are collected in snapshot matrices of the form shown in Eq. (2), we use the DMD algorithm [5], to obtain a linear ROM of the form (4). We then compute the quadratic closure and form the linear-quadratic ROM using Algorithm 1; note we do not employ regularization for this problem. Fig. 2 shows approximated trajectories for ROMs of size $r = 2$ for both DMD and the proposed approach of DMD plus quadratic closure. Fig. 2a depicts the linear subspace in which DMD approximates the trajectory, while Fig. 2b depicts how the closure brings in a component of the approximation the third dimension (i.e., the dimension orthogonal to the linear subspace shown in Fig. 2a). For this example, the quadratic closure term leads to approximately 50% reduction in the approximation error integrated over the trajectory. Fig. 2b also illustrates that because the linear-quadratic ROM still only has two degrees of freedom, the three-dimensional trajectory cannot be represented exactly. Clearly in this example, one would prefer to take the extra dimension as a full degree of freedom—it is important to note that we would not advocate for the quadratic closure approach in such a case. Rather, the example is presented to give an intuitive geometric picture of how the approach works.

III. Results

In this section, we demonstrate the predictive capabilities of the proposed approach on two examples. The first is a numerical simulation of Burgers' equation.The second is an experimental dataset of time-resolved particle image

(a) DMD: linear subspace approximation

(b) DMD plus quadratic closure
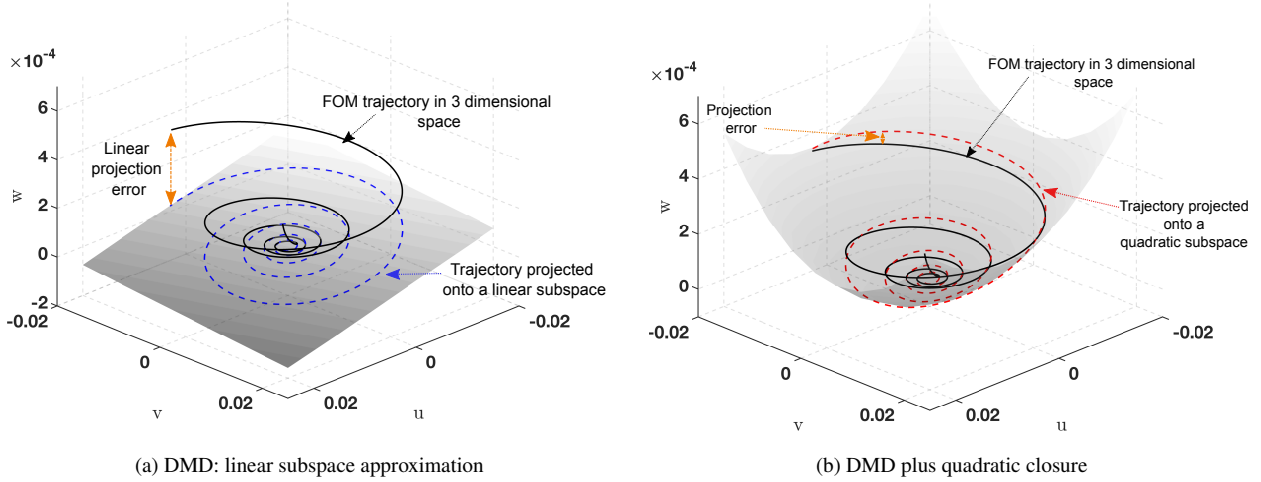
Fig. 2 Geometric depiction on cylinder wake example from [31], showing ROMs of state dimension $r = 2$ developed using (a) DMD and (b) the proposed approach of DMD plus a quadratic closure.

velocimetry (TR-PIV) data obtained from the flowfield of helicopter blades. The ROMs for the Burgers' equation example are developed for two cases (i) a low-data regime and (ii) a sufficient-data regime. However, since it is typical to have access to limited measurements for the experimental datasets, we evaluate the ROM's performance only in the low-data regime in the experimental data example. We demonstrate that when sufficient data are available, all the ROMs developed demonstrate similar performance, while in the low-data regime, the proposed approach displays improved predictive performance.

A. Numerical dataset: Burgers' Equation

The dynamics of a soliton (solitary wave) on a spatial domain $\Omega = [0, 1]$ for a given field $u(y, t)$, where $y \in \Omega$ and t are the spatial and temporal dimension is described by Burgers' equation

$$\frac{\partial}{\partial t}u(y, t) + u(y, t)\frac{\partial}{\partial t}u(y, t) = v\frac{\partial^2}{\partial y^2}u(y, t), \tag{14}$$

where v is the viscosity of the fluid, set here to $v = 0.001$. In this section, the initial condition for the simulations is $u(y, 0) = sin(4\pi y)$. Homogeneous boundary conditions are imposed such that $u(0, t) = u(1, t) = 0$. The spatial domain y is discretized with an equidistant grid of $N = 1024$ points and the temporal domain has an incremental time step of $\Delta t = 10^{-3}$ resulting in a total of 500 snapshots of data. The resulting spatial-temporal evolution of the low-viscosity regime soliton wave is shown under the FOM tile in Fig. 3. Here, the formation of shocks can be observed at $t = 0.1$ time units.

The primary aim of this work is to improve the predictive capabilities of the developed ROMs. To demonstrate the improved predictive capability of the ROMs, we train the ROMs in three separate cases: (i) insufficient-data regime,

9

(ii) low-data regime and (iii) sufficient-data regime. In the insufficient-data regime, the ROMs are trained on 10% of available data. In the low-data regime and sufficient-data regime, we train using 20% and 30% of the available snapshot data, respectively. For all three cases, the end of the training regime is marked by a red dashed line in Fig. 3. The ROMs are developed by retaining $r = 3$ POD modes; this corresponds to retaining 99.99%, 99.98% and 99.97% of the total energy contributed from the available snapshot data for cases (i), (ii) and (iii), respectively. As described in Sec. II, the resulting DMD and proposed approach have linear and linear-quadratic structure ROMs, respectively.
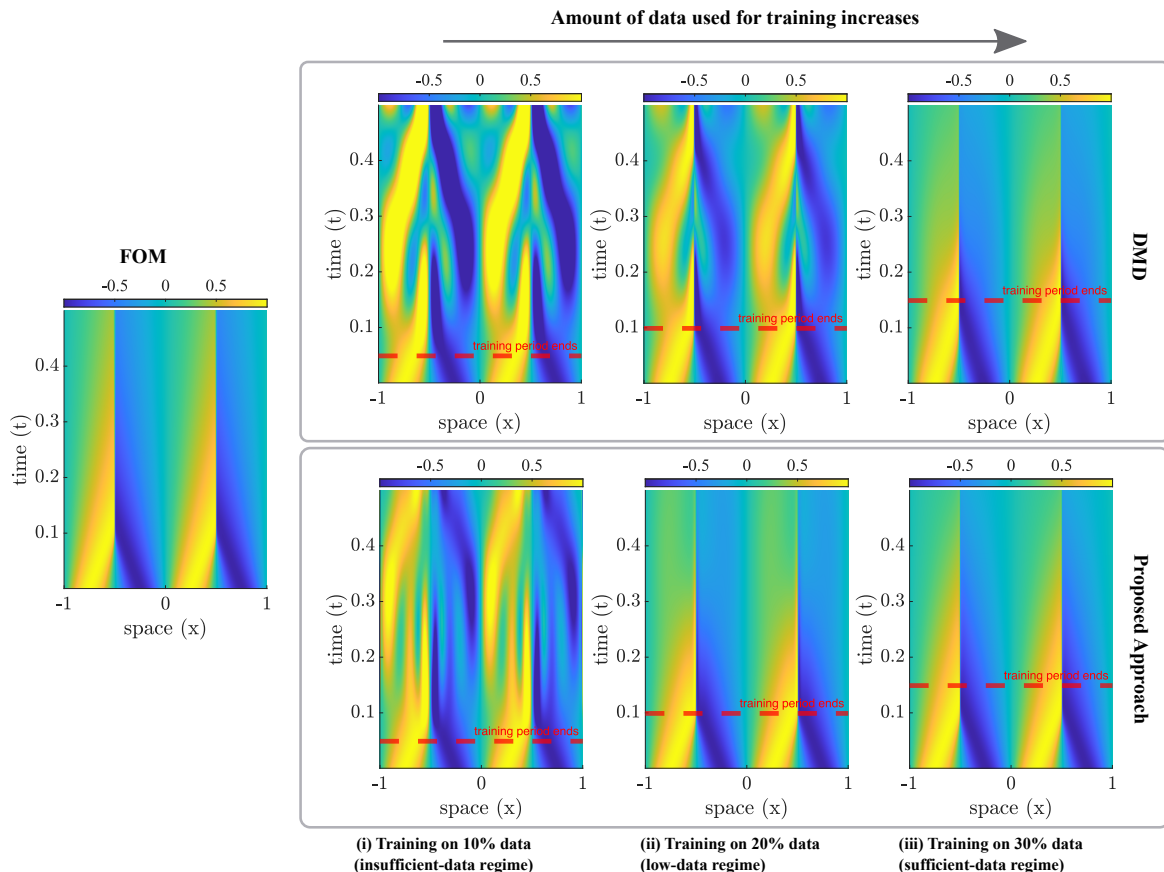
Fig. 3   The space-time state solution for the low-viscosity Burgers' equation is shown for the full-order model in the leftmost tile. The columns (from left to right) correspond to the (i) insufficient-data regime with training on 10% of data available, (ii) low-data regime with training on 20% of data available, and (iii) sufficient-data regime with training on 30% of data available. The top row shows the DMD ROMs, while the bottom row shows the ROMs with quadratic closure using the proposed approach.

Figure 3 demonstrates the training and predictive capability of ROMs of size $r = 3$. The full-order model is shown separately on the left-most tile titled FOM, the top row corresponds to the DMD ROMs, and the bottom row corresponds to the DMD ROMs with quadratic closure. For each row, moving from left to right corresponds to ROMs that are built on an increasing amount of training data. All the ROMs do well to reconstruct their respective training data; however, they have varying performance in their predictive capability. In (i) the insufficient-data regime (left column), it can be

seen that the training data does not include formation of the shock and hence both ROMs perform poorly. In (ii) the low-data regime (middle column), the training regime ends as the formation of the shock begins. Here, we observe that the DMD ROM (top row) does not generalize well beyond the training data regime. In contrast the DMD with quadratic closure (bottom row) is more robust and predicts the evolution of the flowfield with reasonable accuracy. In the sufficient-data regime (right column), both ROMs perform well in predicting the dynamics beyond the training regime. For obtaining these results using Algorithm 1, we select the best regularization parameter, that is γ, by solving the optimization problem over a grid of 50 logarithmically spaced regularization values in the range $[10^{-4}, 10^2]$.

Fig. 4a shows the relative state errors as a function of ROM state dimension, r, for the ROMs trained in the low-data and sufficient-data regimes. The relative errors are evaluated separately for training (solid lines) and testing (dashed lines) snapshot datasets. We observe that the proposed approach, in both the low-data and sufficient-data regime, has lower training and testing errors compared to DMD. In addition, we also plot the lower-bound for the testing error, which is defined as $\frac{\|\mathbf{X}_{\text{test}} - \mathbf{U}_r \mathbf{U}_r^\top \mathbf{X}_{\text{test}}\|_F}{\|\mathbf{X}_{\text{test}}\|_F}$, where $\mathbf{X}_{\text{test}}$ is the testing regime snapshot matrix.

Two important points must be emphasized. First, the linear DMD ROMs are computationally faster to solve than the linear-quadratic ROMs, because of the extra computational cost in computing the quadratic closure term. In both cases, the ROMs are solved in a fraction of a second ($\approx O(10^{-6})$ seconds wall clock time for the DMD ROMs and $\approx O(10^{-5})$ seconds for the linear-quadratic ROMs), and so the differences are small, but this may be an important consideration for some applications. Second, this Burgers' example has been architected to show a failure of DMD. The vast literature shows that DMD works robustly across a broad range of problems—in such cases it would be the preferred method. However, these results do illustrate the potential pitfalls of deriving ROMs when limited training data are available. In such situations, a DMD ROM may not necessarily improve by simply increasing the number of modes. In this Burgers' example, we see instabilities introduced by Gibbs oscillations as higher-order modes are included. In such situations, keeping the number of DMD modes low and adding a quadratic closure term may provide more robustness and thus a better predictive performance.

B. Experimental dataset: Rotorcraft flowfield in hover

This section's aim is to obtain ROMs that model dynamics of fluid-structure interaction between a rotor blade and surrounding air, using experimental datasets. While many works have developed ROMs using experimental datasets in the DMD literature, some useful references without claim to completeness are [5, 32, 33]. The following subsection briefly describes the experimental setup used to obtain the experimental data. This is followed by results that demonstrate the performance of the ROMs using the available experimental data.
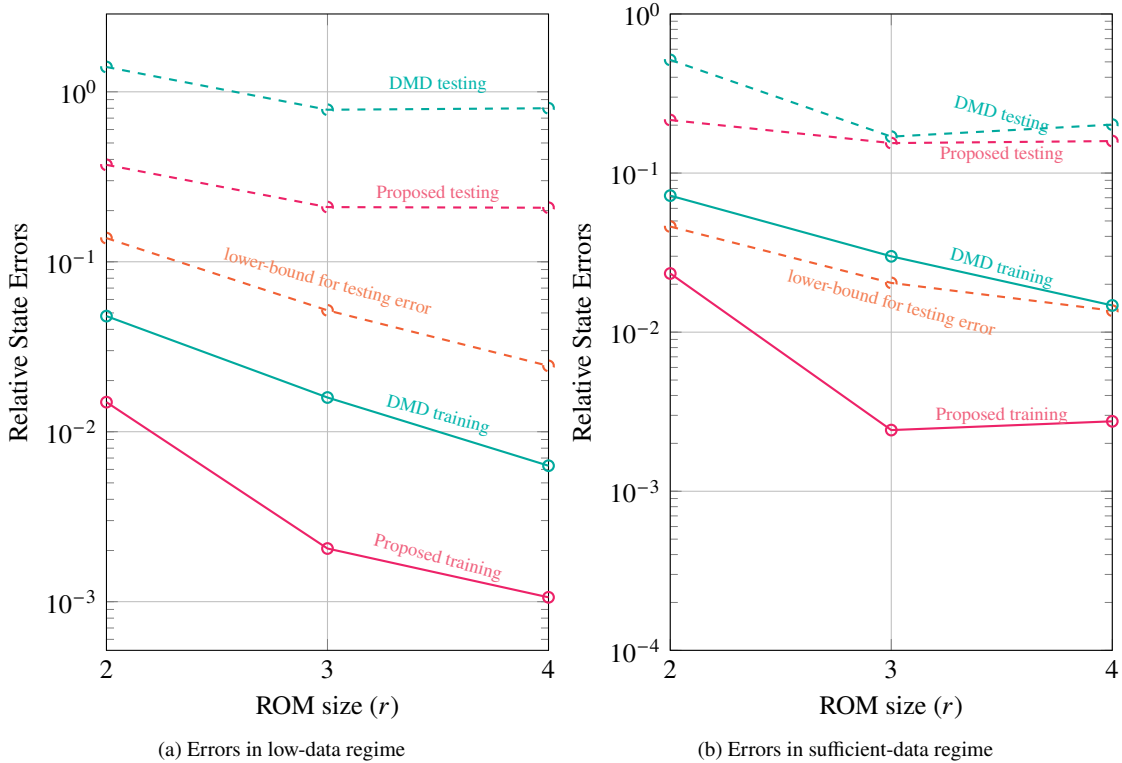
Fig. 4 **Relative state errors for ROM predictions over training and testing datasets for Burgers' equation. Left: low-data regime (20% snapshot data). Right: sufficient-data regime (30% snapshot data).**

1. Experimental setup

All experimental measurements were performed indoors at the University of Texas at Austin rotor test facility. The test stand in Fig. 5a was located in a large test chamber $(15.24 \times 10.06 \times 18.30)$ m. The rotor shaft was oriented horizontally with thrust directed toward the test stand so that the rotor wake was unobstructed. The rotor consisted of two constant-chord, untwisted blades on a rigid rotor hub (no flap or lag hinges). The rotor blades had a modified VR-12 airfoil with 5% trailing edge tab. Rotor parameters are listed in Table 1.

Flowfield measurements were performed in hover at a nondimensional thrust coefficient of $C_T = 0.06$, and a rotational speed of 900 RPM corresponding to a blade tip Mach number of $M = 0.3$ and a chord Reynolds number of $Re_{\text{tip}} = 562,000$ at the rotor blade tip. The thrust condition is written as a nondimensional coefficient $C_T = T\rho\pi\Omega^2 R^4$, where ρ is the density, R is the rotor radius, and Ω is the rotor speed. The thrust condition provides an accurate reference for other experiments with different rotor geometries. The flowfield was measured by time-resolved two-dimensional-two-component (2D-2C) particle image velocimetry (PIV), using two 4-megapixel high-speed Phantom VEO-640 cameras in conjunction with a Photonics dual-pulsed ND:YLF laser (527nm, 30mJ/pulse). Each camera viewed an independent field of view (FOV). One camera captured the inboard region of the rotor blade, while the second camera captured the blade tip region. These two FOVs were merged together to give the flowfield in a single region of

interest (ROI), shown in Fig. 5c. The origin of the images ($z = 0$ and $r = 0$) was located at the center of the rotor hub. An optical encoder mounted on the main rotor shaft provided a consistent timing signal for triggering the time-resolved measurements. The time-resolved measurements were made at 41/revolution corresponding to an azimuthal angle increment of $\Delta\psi = 8.8°$. A total of 820 images are available for training and testing purposes.

(a) Experimental setup for time-resolved PIV data

(b) Region of interest (ROI)

(c) PIV image of ROI
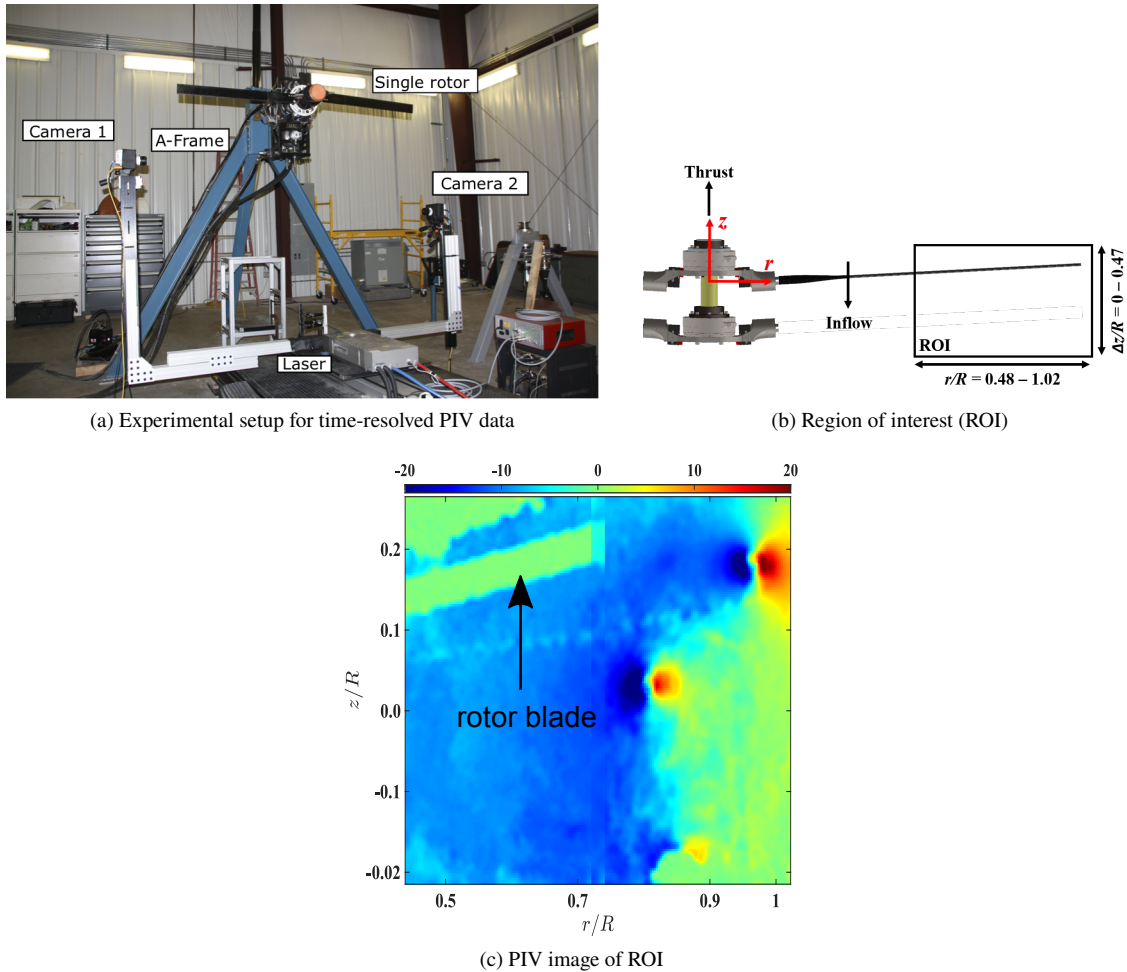
Fig. 5   The figure in (a) shows the experimental setup, in (b) the region of interest of the blade that is captured by the camera is shown, and in (c) the time-resolved PIV data used for developing ROMs.

An important point is that centering the data with a reference matrix $\mathbf{X}_{\text{ref}} \in \mathbb{R}^{N \times k}$, such that the centered snapshot is $\mathbf{X}_{\text{cent}} := \mathbf{X} - \mathbf{X}_{\text{ref}}$, can be beneficial. As noted in [16], choosing an appropriate reference is important when using a quadratic manifold. The matrix $\mathbf{X}_{\text{ref}}$ is typically used to account for changes in initial conditions, shifting equilibrium points, or centering the data about a mean. In this work, the data is centered around the mean of the snapshot matrix and is normalized by the maximum value.

Table 1   Rotor parameters

Blade Airfoil		VR-12
Radius	R	1.108m
Chord	c	0.080m
Root Cutout	r_a	$19\%R$
Precone Angle	β_0	$3°$

2. Results

In this section, we develop ROMs for the flowfield of the rotor in hover. The main goal of developing ROMs for this problem is to have predictive ROMs that can identify important large-scale flow structures, such as the rotor blade tip vortices that convect downwards in the flow, and that can model the development of the wake over time. To develop these ROMs, we use 30% of the available 820 snapshots for training, so that we have k_{train} = 245. The remaining snapshots are used for testing. Based on singular value decay, we choose a ROM size of r = 14. The convection of the vortices downwards makes this problem challenging to predict. We compare the results for training and predictions for ROMs obtained from DMD and the proposed method of DMD with a quadratic closure.

To assess the effectiveness of the ROMs developed, we analyze the instantaneous y-component of velocity. In Fig. 6, it can be observed that both the linear and linear-quadratic ROMs yield a good reconstruction of the training dataset, where both the rotor blade passage and the positions of blade tip vortices are reconstructed. Fig. 7 shows the prediction regime for the same ROMs. Here again, the quantities of interest (i.e., the tip vortices) are identified by both ROMs accurately. While the older tip vortex is identified using the ROMs, its intensity is not represented as expected. To quantify the performance of the reconstruction, we study the phase-averaged velocity obtained from the two ROMs shown in Fig. 8. We select four positions at $z/R = -0.078, -0.15, 0.05, 0.078$, and plot the averaged velocity over r/R. For all the above listed z/R positions, we plot the average velocity, $\mathbf{v}_{\text{ax}}$, from the proposed approach (in red) and the DMD-ROM (in green), while the experimental data are shown in black. In Fig. 8a, at $z/R = -0.078$, it can be seen that the DMD ROM with quadratic closure follows the experimental data well in the region $r/R = 0.5$ to $r/R = 0.7$ and $r/R = 0.85$ to $r/R = 1.0$; this is the same region where large-scale structures exist and have been effectively identified. In all the plots in Fig. 8, we see that the averaged velocities of the proposed approach in the region $r/R = 0.75$ to $r/R = 0.85$ closely track that of the experimental dataset's velocity.

IV. Conclusions

This work proposes a method for augmenting DMD ROMs with a quadratic closure term. The approach can be interpreted as projection of a large linear DMD model onto a quadratic manifold of smaller dimension. The quadratic manifold is learned from snapshot data by solving a scalable linear least-squares problem. The quadratic closure term represents contributions of modes that are neglected in the reduced-order representation. The approach may be

14
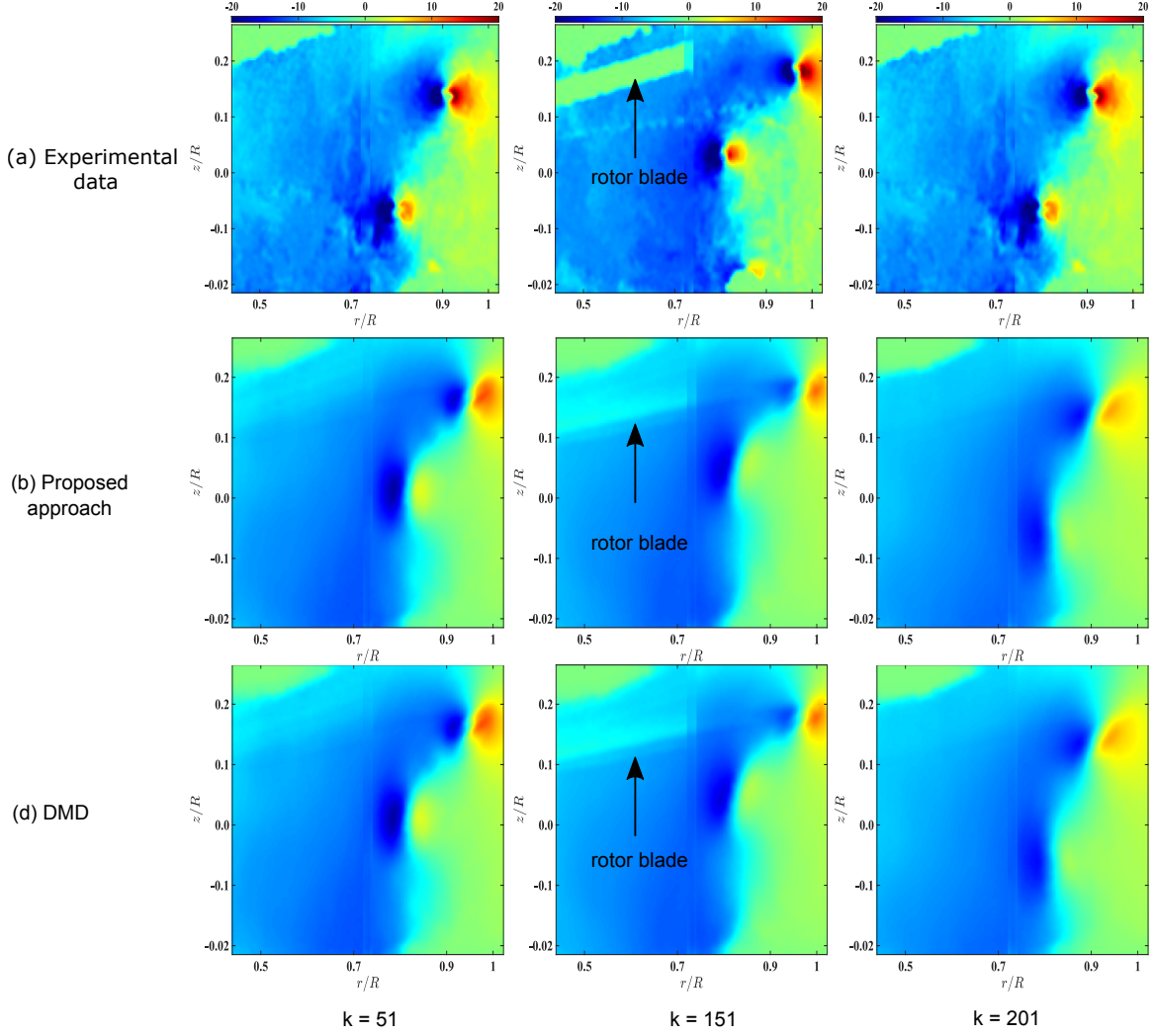
Fig. 6 Flowfield for (a) experimental data and ROMs of size $r = 14$ **using (b) the proposed approach of DMD plus quadratic closure and (c) linear DMD. The training snapshots are shown for** $k = 51, \, 151, \, 201$.

beneficial in situations where including higher-order POD modes in the linear subspace leads to instability in the ROM. This was illustrated through a convectively dominated Burgers' equation example, where instabilities introduced by Gibbs oscillations corrupt the DMD ROM as higher-order modes are included in the linear subspace. In contrast, the closure term allows for the ROM's dynamics to include components associated with higher-order modes, but the modal coefficients for the higher-order modes are constrained to be quadratic functions of the modal coefficients of the low-order modes. For the Burgers' example studied in this paper, this permitted accurate, stable ROMs in cases where DMD fails to provide accurate predictions outside of the training regime. Further, the proposed approach outperformed DMD in creating a ROM from an experimental dataset of the flowfield of a rotor in hover.
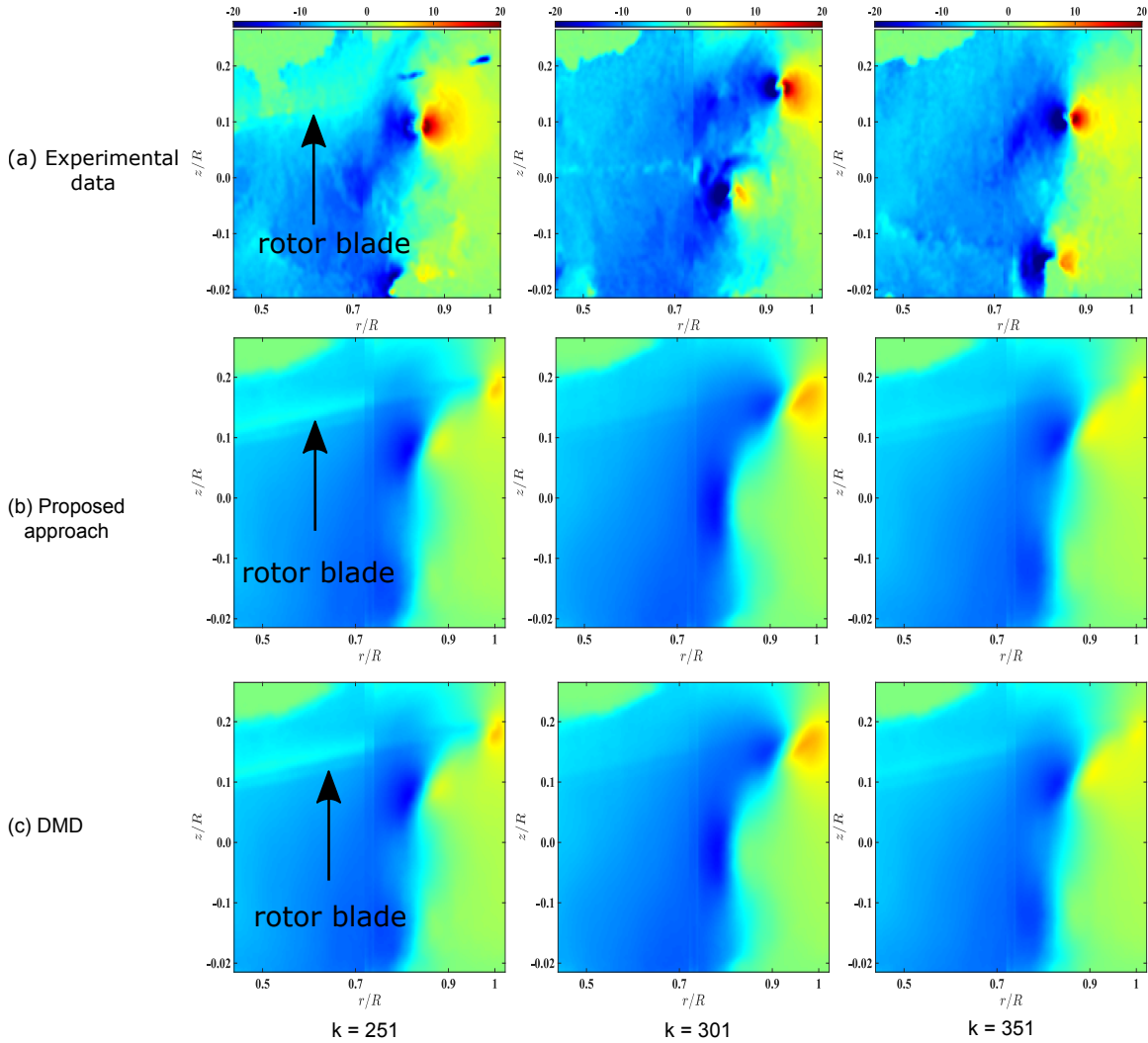
Fig. 7 Flowfield for (a) experimental data and ROMs of size $r = 14$ **using (b) the proposed approach of DMD plus quadratic closure and (c) linear DMD. The testing snapshots are shown for** $k = 251, \ 301, \ 351$**. The vortices are quantities of interest to be identified in the prediction regime.**

V. Acknowledgments

References

[1] Rowley, C. W., and Dawson, S. T. M., "Model Reduction for Flow Analysis and Control," *Annual Review of Fluid Mechanics*, Vol. 49, 2017, pp. 387–417. https://doi.org/10.1146/annurev-fluid-010816-060042.

[2] Benner, P., Gugercin, S., and Willcox, K., "A Survey of Projection-Based Model Reduction Methods for Parametric Dynamical Systems," *SIAM Review*, Vol. 57, No. 4, 2015, pp. 483–531. https://doi.org/10.1137/130932715.

[3] Lumley, J. L., "The structure of inhomogeneous turbulent flows," *Atmospheric Turbulence and Radio Wave propagation*, 1967, pp. 166–178.

[4] Holmes, P., Lumley, J., Berkooz, G., and Press, C. U., *Turbulence, Coherent Structures, Dynamical Systems and Symmetry*, Cambridge Monographs on Mechanics, Cambridge University Press, 1996.

[5] Schmid, P. J., "Dynamic mode decomposition of numerical and experimental data," *Journal of Fluid Mechanics*, Vol. 656, 2010, p. 5–28. https://doi.org/10.1017/S0022112010001217.

[6] Tu, J. H., Rowley, C. W., Luchtenburg, D. M., Brunton, S. L., and Kutz, J. N., "On dynamic mode decomposition: Theory and applications," *Journal of Computational Dynamics*, Vol. 1, No. 2, 2014, pp. 391–421.

[7] Taira, K., Brunton, S. L., Dawson, S. T. M., Rowley, C. W., Colonius, T., McKeon, B. J., Schmidt, O. T., Gordeyev, S., Theofilis, V., and Ukeiley, L. S., "Modal Analysis of Fluid Flows: An Overview," *AIAA Journal*, Vol. 55, No. 12, 2017, pp. 4013–4041. https://doi.org/10.2514/1.J056060.

[8] Taira, K., Hemati, M. S., Brunton, S. L., Sun, Y., Duraisamy, K., Bagheri, S., Dawson, S. T. M., and Yeh, C.-A., "Modal Analysis of Fluid Flows: Applications and Outlook," *AIAA Journal*, Vol. 58, No. 3, 2020, pp. 998–1022. https://doi.org/10.2514/1.J058462.

[9] Hemati, M. S., Williams, M. O., and Rowley, C. W., "Dynamic mode decomposition for large and streaming datasets," *Physics of Fluids*, Vol. 26, No. 11, 2014. https://doi.org/10.1063/1.4901016.

[10] Zhang, H., Rowley, C. W., Deem, E. A., and Cattafesta, L. N., "Online Dynamic Mode Decomposition for Time-Varying Systems," *SIAM Journal on Applied Dynamical Systems*, Vol. 18, No. 3, 2019, pp. 1586–1609. https://doi.org/10.1137/18M1192329.

[11] Brunton, S. L., Proctor, J. L., and Kutz, J. N., "Discovering governing equations from data by sparse identification of nonlinear dynamical systems," *Proceedings of the National Academy of Sciences*, Vol. 113, No. 15, 2016, pp. 3932–3937. https://doi.org/10.1073/pnas.1517384113.

[12] Rudy, S. H., Brunton, S. L., Proctor, J. L., and Kutz, J. N., "Data-driven discovery of partial differential equations," *Science Advances*, Vol. 3, No. 4, 2017, p. e1602614. https://doi.org/10.1126/sciadv.1602614.

[13] Peherstorfer, B., and Willcox, K., "Data-driven operator inference for nonintrusive projection-based model reduction," *Computer Methods in Applied Mechanics and Engineering*, Vol. 306, 2016, pp. 196–215. https://doi.org/https://doi.org/10.1016/j.cma.2016.03.025.

[14] Qian, E., Kramer, B., Peherstorfer, B., and Willcox, K., "Lift & Learn: Physics-informed machine learning for large-scale nonlinear dynamical systems," *Physica D: Nonlinear Phenomena*, Vol. 406, 2020, p. 132401. https://doi.org/https://doi.org/10.1016/j.physd.2020.132401.

[15] McQuarrie, S. A., Huang, C., and Willcox, K. E., "Data-driven reduced-order models via regularised operator inference for a single-injector combustion process," *Journal of the Royal Society of New Zealand*, Vol. 51, No. 2, 2021, pp. 194–211.

[16] Geelen, R., Wright, S., and Willcox, K., "Operator inference for non-intrusive model reduction with quadratic manifolds," *Computer Methods in Applied Mechanics and Engineering*, Vol. 403, 2023, p. 115717. https://doi.org/https://doi.org/10.1016/j. cma.2022.115717.

[17] Lee, K., and Carlberg, K. T., "Model reduction of dynamical systems on nonlinear manifolds using deep convolutional autoencoders," *Journal of Computational Physics*, Vol. 404, 2020, p. 108973. https://doi.org/https://doi.org/10.1016/j.jcp.2019. 108973.

[18] Pawar, S., San, O., Rasheed, A., and Vedula, P., "A priori analysis on deep learning of subgrid-scale parameterizations for Kraichnan turbulence," *Theoretical and Computational Fluid Dynamics*, Vol. 34, No. 4, 2020, pp. 429–455.

[19] Ahmed, S. E., San, O., Rasheed, A., and Iliescu, T., "Nonlinear proper orthogonal decomposition for convection-dominated flows," *Physics of Fluids*, Vol. 33, No. 12, 2021, p. 121702. https://doi.org/10.1063/5.0074310.

[20] Jain, S., Tiso, P., Rutzmoser, J. B., and Rixen, D. J., "A quadratic manifold for model order reduction of nonlinear structural dynamics," *Computers & Structures*, Vol. 188, 2017, pp. 80–94. https://doi.org/https://doi.org/10.1016/j.compstruc.2017.04.005.

[21] Rutzmoser, J., Rixen, D., Tiso, P., and Jain, S., "Generalization of quadratic manifolds for reduced order modeling of nonlinear structural dynamics," *Computers & Structures*, Vol. 192, 2017, pp. 196–209. https://doi.org/https://doi.org/10.1016/j.compstruc. 2017.06.003.

[22] Barnett, J., and Farhat, C., "Quadratic approximation manifold for mitigating the Kolmogorov barrier in nonlinear projection-based model order reduction," *Journal of Computational Physics*, Vol. 464, 2022, p. 111348. https://doi.org/https://doi.org/10. 1016/j.jcp.2022.111348.

[23] Wang, Z., Akhtar, I., Borggaard, J., and Iliescu, T., "Proper orthogonal decomposition closure models for turbulent flows: a numerical comparison," *Computer Methods in Applied Mechanics and Engineering*, Vol. 237, 2012, pp. 10–26.

[24] Xie, X., Mohebujjaman, M., Rebholz, L. G., and Iliescu, T., "Data-driven filtered reduced order modeling of fluid flows," *SIAM Journal on Scientific Computing*, Vol. 40, No. 3, 2018, pp. B834–B857.

[25] Pan, S., and Duraisamy, K., "Data-Driven Discovery of Closure Models," *SIAM Journal on Applied Dynamical Systems*, Vol. 17, No. 4, 2018, pp. 2381–2413. https://doi.org/10.1137/18m1177263.

[26] Ahmed, S. E., Pawar, S., San, O., Rasheed, A., Iliescu, T., and Noack, B. R., "On closures for reduced order models – A spectrum of first-principle to machine-learned avenues," *Physics of Fluids*, Vol. 33, No. 9, 2021, p. 091301. https://doi.org/10.1063/5.0061577.

[27] Reyes, R., and Codina, R., "Projection-based reduced order models for flow problems: A variational multiscale approach," *Computer Methods in Applied Mechanics and Engineering*, Vol. 363, 2020, p. 112844. https://doi.org/https://doi.org/10.1016/j. cma.2020.112844.

[28] Kalur, A., Nabi, S., and Benosman, M., "Robust Adaptive Dynamic Mode Decomposition for Reduce Order Modelling of Partial Differential Equations," *American Control Conference (ACC)*, 2021, pp. 4497–4502. https://doi.org/10.23919/ACC50511.2021.9483319.

[29] Rowley, C. W., Mezic, I., Bagheri, S., Schlatter, P., and Henningson, D. S., "Spectral analysis of nonlinear flows," *Journal of Fluid Mechanics*, Vol. 641, 2009, p. 115–127. https://doi.org/10.1017/S0022112009992059.

[30] Mezic, I., "Analysis of fluid flows via spectral properties of the Koopman operator," *Annual Review of Fluid Mechanics*, Vol. 45, No. 1, 2013, pp. 357–378.

[31] Noack, B. R., Afanaseiv, K., Morzyński, M., Tadmor, G., and Thiele, F., "A hierarchy of low-dimensional models for the transient and post-transient cylinder wake," *Journal of Fluid Mechanics*, Vol. 497, 2003, p. 335–363. https://doi.org/10.1017/S0022112003006694.

[32] Hemati, M. S., Rowley, C. W., Deem, E. A., and Cattafesta, L. N., "De-biasing the dynamic mode decomposition for applied Koopman spectral analysis of noisy datasets," *Theoretical and Computational Fluid Dynamics*, Vol. 31, No. 4, 2017, pp. 349–368. https://doi.org/10.1007/s00162-017-0432-2.

[33] de Lamotte, A., Delafosse, A., Calvo, S., and Toye, D., "Analysis of PIV measurements using modal decomposition techniques, POD and DMD, to study flow structures and their dynamics within a stirred-tank reactor," *Chemical Engineering Science*, Vol. 178, 2018, pp. 348–366. https://doi.org/https://doi.org/10.1016/j.ces.2017.12.047.

(a) $z/R = -0.078$

(b) $z/R = 0.078$

(c) $z/R = -0.15$

(d) $z/R = -0.05$
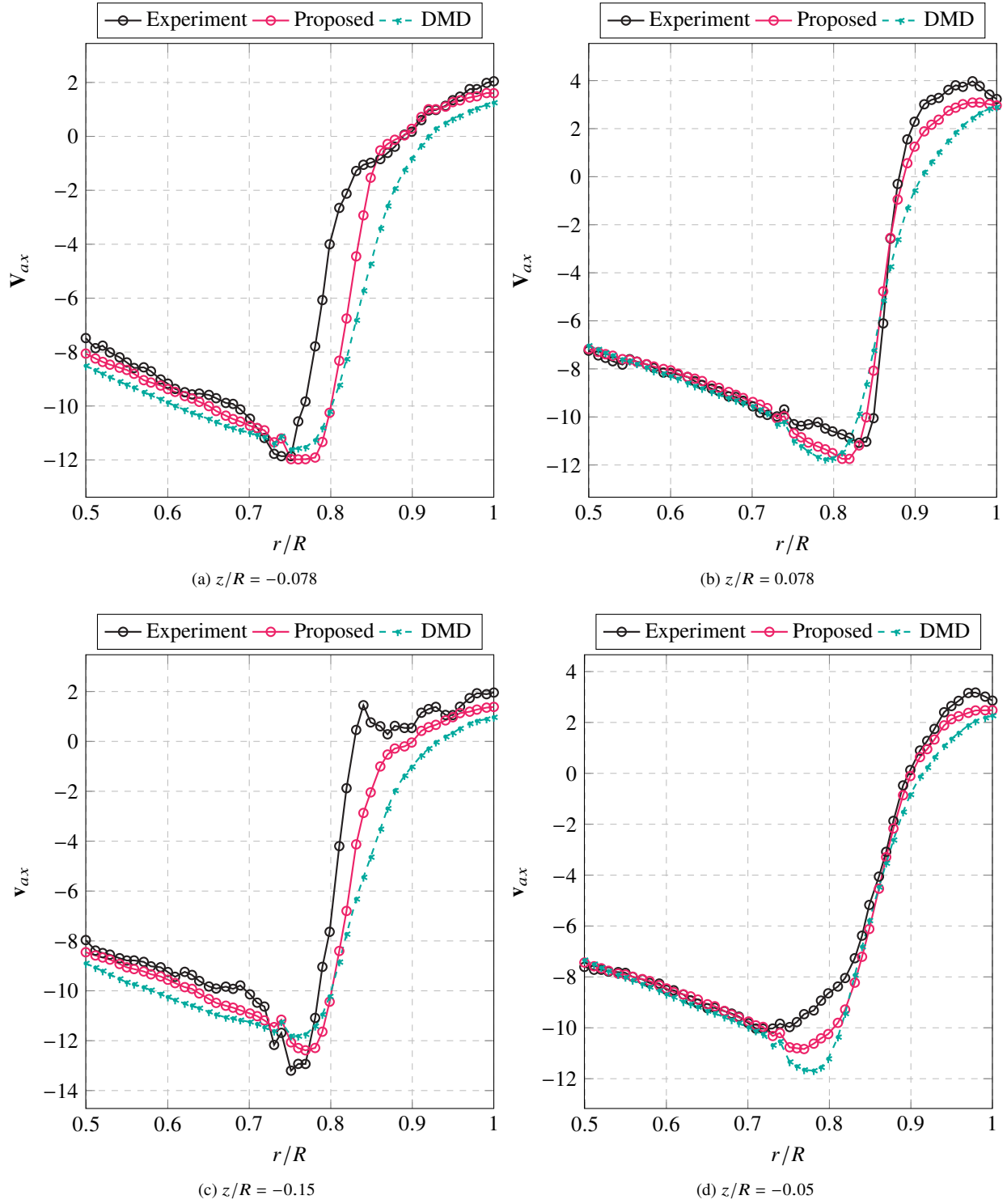
Fig. 8 **The variation of phased average velocity over r/R at four different z/R locations for ROM size $r = 14$. It can be seen that the proposed approach at different z/R locations follows the experimental data closely.**